Graphene Oxide-Polydopamine Derived N, S-codoped Carbon Nanosheets as Superior Bifunctional Electrocatalysts for Oxygen Reduction and Evolution

Konggang Qu, Yao Zheng, Sheng Dai and Shi Zhang Qiao**

[*] Dr. K. G. Qu, Dr. Y. Zheng, Prof. S. Dai, and Prof. S. Z. Qiao.

School of Chemical Engineering,

The University of Adelaide,

Adelaide, SA, 5005, Australia

E-mail: s.qiao@adelaide.edu.au; s.dai@adelaide.edu.au

Keywords: mesoporous carbon nanosheets, nonmetallic codoping, oxygen reduction (ORR), oxygen evolution (OER), bifunctional, electrocatalysis.

Abstract:

Engineering carbon materials as the bifunctional catalysts for both electrocatalytic oxygen reduction/evolution reactions (ORR/OER) is highly promising for the large-scale commercialization of regenerative fuel cells and rechargeable metal-air batteries. Codoping carbons with heteroatoms can achieve unique electronic structures and show tailored electrocatalytic capabilities by rationally regulating their dopants. Sulfur is one of the most important dopants from both experimental and theoretical perspectives. In this work, a novel, highly efficient and environmentally benign method for sulfur incorporation into carbon framework has been developed facilely on the basis of graphene oxide-polydopamine (GD) hybrids to derive the N, S-codoped mesoporous carbon nanosheets. 16.7 at. % S can be conjugated to the GD hybrids associated with the S doping efficiency up to 6.1% after 800 ^{o}C pyrolysis, which is higher than most previous S doping approaches. The resultant N, S-codoped mesoporous carbon nanosheets exhibit superior performance with favorable kinetics and excellent durability as a bifunctional ORR and OER catalyst, which is much better than that of most reported metal-free doped carbon, even transition metal and noble metal catalysts. The high concentrations of multiple dopants, abundant porous architecture and good electron transfer ability are believed to significantly expedite the ORR and OER catalytic processes. In the light of physicochemical versatility and structural tunability of polydopamine (PDA), this work provides a universal platform towards further development of PDA-based carbon materials with heteroatom dopants as the highly efficient electrocatalysts.

Introduction

Regenerative fuel cells and rechargeable metal-air batteries have drawn intensive attention in energy storage and conversion applications due to their theoretically high energy densities.[1] The reaction rates of cathodic oxygen reduction reaction (ORR) and anodic oxygen evolution reaction (OER) as half reactions play key roles in the output performance of these devices. However, the sluggish kinetics of both ORR and OER have posed many scientific challenges due to their complicated multi-electron transfer processes resulting relative high overpotentials [1,2]. The common electrocatalysts based on noble metals like Pt, Ir, and Ru, *etc.* are usually effective to boost the ORR or OER rates, but their practical applications are severely hindered by the prohibitive cost, scarce resource, and poor durability [3-6]. Therefore, extensive studies have been dedicated to searching for alternative catalysts to replace noble metals with comparable electrocatalytic activity yet acceptable cost [7-10]. Recently, the state-of-the-art non-metallic heteroatom-doped carbon materials have aroused tremendous interests because of their competitive activity, low cost and significantly enhanced stability [11-14]. Among these materials, the approach of codoping two or more selected heteroatoms into the designed sites of carbon matrix is becoming one of the major trends nowadays, because it can create a unique electronic structure with synergistic coupling effect among heteroatom dopants [15-17]. These codoped carbon materials not only are more catalytically active than most single doped carbon, but also show tailored catalytic capabilities for different electrocatalytic reactions by altering doping types, sites and levels. For example, N, B or N, S-codoped graphene reveals much better ORR performance [16,18,19], while N, O-codoped carbon hydrogels show noticeable catalytic activity for the OER [20]. Therefore, the possibility of codoped carbon materials as the bifunctional catalysts for both ORR and OER is highly promising by rationally regulating their dopants.

Sulfur is one of the most important dopants to tailor the electrocatalytic activities of carbons, from both experimental and theoretical perspectives [16,21-24]. The conventional strategies reported for

preparing codoped carbons with S (mostly N, S-codoped carbons) involve a thermal evaporation/vaporization process, i.e. heating carbon materials (graphene, carbon nanotube, etc) in the gas atmosphere containing N and S (NH_3, pyridine, H_2S, SO_2, and thiophene) [23,24] or with some precursors (melamine, benzyl disulfide) [16] that can be pyrolyzed into gases at high temperature. However, there are some limitations arising from these post-treatment doping approaches. For example, although excessive N and S sources (e.g. melamine and benzyl disulfide) and high temperature (> 900 ºC) are used, the doping efficiency is still very low (< 5 at. %). More seriously, vast majority of raw materials are discharged in the form of N or S-bearing waste gases, which is apparently not environmentally benign [16,23]. On the other hand, pyrolysis of rich N-containing precursors has been widely used for the fabrication of N-doped carbon materials which can greatly improve the doping efficiency of nitrogen [13,17,25]. However, this method is not practically applicable for the preparation of N, S-codoped materials in view of the high cost and the scarcity of N, S-containing precursors [26].

Recently, we used polydopamine (PDA) as the N-containing precursors to derive mesoporous carbon nanosheets as an efficient ORR catalyst [27]. Compared with other commonly used N-containing precursors such as melamine [13], polypyrrole [17], and polyaniline[25,28], PDA displays many incomparable features. For example, PDA is nontoxic, extrmely soluble and has a high carbon yield [29]; PDA also has excellent structural tunability and strong chelation capability to metal ions, implying the possibility of fabricating many desired nanostructures with adjustable components [29-33]. The most important is the facile post-modification of PDA; PDA is particularly reactive to amine or thiol groups *via* Schiff base or Michael addition reaction [34-37]. Especilly, the thiol addition reaction proceeds extremely fast with its rate constants ranging from 4×10^5 to 3×10^7 M^{-1} s^{-1} (in the case of cysteine at pH =7) [38]. These reactions proceed efficiently at room temperature without need of any harsh reaction condition. Therefore, it is particularly advantageous to prepare codoping carbon materials using the PDA as the N-containing precursor since a variety of

heteroatoms including nitrogen and sulfur can be easily introduced via the post-modification of PDA. The above unique and remarkable features make PDA highly promising as a simple and effective candidate for the preparation of N, S-codoped functional carbon materials. Although PDA has been extensively serviced as the building block to construct metallic or non-metallic composites based on its remarkable physicochemical versatility [39,40], few relevant eletrocatalytical works have been reported [41,42].

Herein, we use graphene oxide and PDA to derive the N, S-codoped carbon sheets as the highly efficient bifunctional electrocatalysts for ORR and OER. Graphene oxide (GO) is used as the substrate to synthesize sulphur modified GO-PDA (GDS) hybrids, where dopamine (DA) polymerizes on the surface of GO to produce a uniform PDA layer, and 2-mercaptoethanol is then conjugated to the PDA through Schiff base or Michael addition reactions. The N, S-codoped mesoporous carbon nanosheets obtained from the pyrolysis of GDS hybrids possess a much higher S-doping efficiency with the assistance of PDA than most reported methods and exhibit excellent ORR/OER bifunctional activity and durability, even better than that of transition-metal and noble metal catalysts. This proof-of-concept study would lay a solid foundation for the further exploration and development of nanostructural PDA-based carbon materials for energy-relevant applications.

Experimental Section

Materials

Natural graphite flakes, sulfuric acid (H_2SO_4, 95-98 %), potassium permanganate ($KMnO_4$, 99 %), phosphorous acid (H_3PO_4, 85 %), hydrogen peroxide (30 %), dopamine hydrochloride, 2-mercaptoethanol and disodium hydrogen phosphate (Na_2HPO_4) were purchased from Sigma-Aldrich and directly used without further purification. Milli-Q water (18.2 MΩ) was used throughout all experiments.

Materials characterization

Fourier transform infrared (FTIR) spectra were collected on the transmission module of a Thermo Nicolet 6700 FTIR spectrometer at 2 cm^{-1} resolution and 64 scans. The transmission electron microscopy (TEM) images were acquired on a JEM-2100 microscopy. TEM elemental mapping was obtained through the EDAX detector attached to the JEM-2100. Atomic force microscopy (AFM) images were acquired under ambient conditions with Ntegra Solaris AFM (NT-MDT) operated in a tapping mode. Scanning electron microscopy (SEM) images were recorded on the FEI Quanta 450 at high vacuum with an accelerating voltage of 10 kV. The Raman spectra were collected on iHR550 from HORIBA Scientific with a 532 nm solid laser as the excitation source. X-Ray diffraction (XRD) was performed on the Miniflx-600 (Rigaku Ltd.) using a Cu Kα X-ray. The X-ray photoelectron spectroscopy (XPS) analysis was conducted on Axis Ultra spectrometer (Kratos Analytical Ltd.) with monochromated Al Kα radiation at ca. 5×10^{-9} Pa. Nitrogen adsorption-desorption isotherm was collected on the Tristar II (Micrometrics) at 77 K. Pore size distribution (PSD) was obtained by Barrett-Joyner-Halenda (BJH) model using the adsorption branch of the isotherm. The specific surface area of the materials was calculated using the adsorption data at the pressure range of P/P_0 = 0.05-0.3 by Brunauer-Emmett-Teller (BET) model.

Preparation of Graphene Oxide (GO)

GO was synthesized from natural graphite flake by an improved Hummers' method with the detailed procedures described in the supplementary materials [43].

Preparation of GO-PDA-S (GDS) hybrids

In a typical experiment, 85 mL GO dispersion (2 mg mL^{-1}) was mixed with 125 mg DA dissolved in 10 mL Milli-Q water. The mixture and another 130 ml Milli-Q water were sonicated for 5 min. Then, 25 mL PBS buffer (0.4 M, pH = 8.5) was added. The mixture was continuously stirred at room temperature for 24 h. After that, 125 mg 2-mercaptoethanol was added and stirred continually for another 12 h. The GDS hybrids were collected by centrifugation and washed for three times with

water. On the other hand, the GO-PDA (GD) hybrids were prepared according to the same procedure but without the addition of 2-mercaptoethanol.

Preparation of N, S-codoped carbon nanosheets (N, S-CNs)

The N, S-CN were prepared through the carbonization of GDS hybrids in a temperature-programmable tube furnace under N_2 atmosphere at 400 ºC for 2 h with a heating rate of 1ºC min^{-1}, which was followed by further treatment at 800 ºC for 3 h with a heating rate of 5 ºC min^{-1}. For the control experiments, the GD hybrids and GO were pyrolyzed under the same condition to obtain the N-doped carbon nanosheets (N-CNs) and reduced GO (rGO).

Electrochemical analysis

For the electrochemical tests, 2 mg of the fabricated catalysts was dispersed in 1 ml of Milli-Q water. The mixture was slightly ultrasonicated to obtain a homogenous catalyst ink. To prepare the working electrode for electrochemical measurements, 20 µl of the ink was dripped on a mirror polished glass carbon electrode. Then, 5 µl of 0.5 wt. % Nafion aqueous solution was dripped on the electrode and dried at room temperature as a binder. After that, the working electrode was inserted into a three-eletrode cell setup, which also included a platinum counter electrode, and an Ag/AgCl/KCl (4 M) reference electrode in a glass cell containing 100 ml of 0.1 M aqueous KOH as an electrolyte. For the ORR and OER, a flow of O_2 was maintained over the electrolyte (0.1 M KOH) during the recording of electrochemical measurements in order to ensure its continued O_2 saturation. The data were recorded using an electrochemical analysisstation (CHI 760C, CH Instruments, USA). More detailed experimental procedures on electrochemical measurements were described in the supplementary materials.

Results and Discussion

As illustrated in Scheme 1, GD hybrids were first synthesized by mixing a given amount of DA with GO in PBS buffer (pH=8.5). DA polymerized to form a PDA thin film directly onto the surface of

GO. 2-mercaptoethanol was then reacted with the PDA *via* the Schiff base or Michael addition reaction to produce the GDS hybrids. PBS buffer was used other than Tris buffer because the primary amine groups of Tris can interact covalently with the PDA, which might influence the deposition of PDA thin films and the ongoing conjugation between 2-mercaptoethanol and PDA [35,37]. The obtained GD and GDS hybrids were pyrolyzed to derive the N-CN and N, S-CN, respectively.

The morphologies and structures of the as-prepared carbon materials were investigated by TEM and AFM. The AFM analyses (Fig. S1A) confirm that PDA forms a uniform coating layer on the surface of GO with the thickness of ~2.5 nm. After grafting 2-mercaptoethanol, the thickness of GDS increases to ~5.0 nm (Fig. S1B). Fig. 1 shows the AFM and TEM images of the obtained N-CN and N, S-CN after 800 ºC pyrolysis. The AFM analysis (Fig. 1A) reveals N-CN has the thickness of ~1.2 nm; TEM image shows N-CN maintains the sheet morphology (Fig. 1B), and the magnified TEM image (Fig. 1C) indicates the N-CN has a smooth surface. AFM image (Fig. 1D) displays the N, S-CN has a thickness of ~3.0 nm. TEM and SEM images (Fig. 1E, S2 & S3) show the N, S-CN has excellent dispersibility and sheet morphology, and abundant crinkles are also observed distinctly on the surfaces. More intriguingly, the N, S-CN displays distinctive and regular porous structure with the size of 3-5 nm while the N-CN does not. It is noteworthy that the porosity of N, S-CN is consistent with that of the N-doped carbon nanosheets reported recently [27], which implies only the hybrid materials with the thickness of 5 nm obtained from GO and PDA can produce porous structures. Nitrogen adsorption isotherms were further used to investigate the surface areas and pore structures of N-CN and N, S-CN. As shown in Fig. 1G, the adsoption-desorption isotherm of N, S-CN displays one distinct hysteresis loop at the relative pressures (P/P_0) from 0.45 to 1.0, which coincides with the type IV classification, suggesting the presence of mesopores. The pore size distribution (PSD) curves further confirm that N, S-CN features highly uniform mesoporous structure with the size centered at 3.6 nm. The BET surface area and the pore volume of N, S-CN are

273.0 m^2 g^{-1} and 0.33 cm^3 g^{-1}, much larger than those of N-CN (62.6 m^2 g^{-1} and 0.06 cm^3 g^{-1}) which have no mesoporous structure. Although the origin of this porosity still needs further study due to the controversial structure of PDA [44,45], this mesoporous architecture is conducive to catalytic processes through the exposure of more active sites and the enhanced diffusion of reactants. Raman spectra of N-CN and N, S-CN (Fig. 1H) dispaly the typical D bands and G bands at roughly 1350 cm^{-1} and 1580 cm^{-1} [46]. The intensity ratio of D band to G band (I_D/I_G) can be conveniently used to estimate the amount of defect and disordered structures. The I_D/I_G ratio increases from N-CN (1.08) to N, S-CN (1.15), which can be attributed to the introduction of extra sulfur atoms and the formation of mesoporous structure of N, S-CN which results in the decomposition of graphitic structure and produces more defects and disordered moieties.

The compositions of the as-prepared carbon materials were detected and analyzed. FTIR verifies the successful deposition of PDA thin film and grafting of 2-mercaptoethanol. As shown in Fig. 2A, the revealed characteristic peaks of GD at 1502 and 1616 cm^{-1} are consistent with the indole or indoline structures of PDA [47,48]. In the case of GDS, the weak peak at 634 cm^{-1} corresponds to the vibration of C-S bond, indicating the successful conjugation of 2-mercaptoethanol. Typical elemental mapping images of N, S-CN (Fig. 2B) illustrate the presence of C, N, S and O elements which are homogeneously distributed on carbon nanosheets. The chemical status of these elements was accurately evaluated by XPS as shown in Fig. 2C & S4. XPS survey scans indicate the presence of carbon, oxygen, nitrogen and sulfur. GDS contains 8.6 % N and 16.7 % S, indicating the high reaction efficiency of thiol addition (Fig. S4), and the N, S-CN retains 4.1 % N and 6.1 % S after pyrolysis (Fig. 2C). It shold be noted that this S-doping efficiency is much higher than that of most reported methods, and a detailed comparison of various S-doping methods is presented in Table S1. Furthermore, due to the strong adhesive ability of PDA to any solid material [33], this effective N, S-codoping method can be used universally to prepare different doped carbon composites. Additionally, the high-resolution N 1s spectra can be deconvoluted into three peaks locating at 398.0, 399.7 and

400.8 eV which can be assigned to pyridinic, pyrrolic and graphitic N (the inset in Fig. 3C). The high resolution S 2p peaks are also deconvoluted, mainly into three peaks associated with C-S-C (163.2 eV for S $2p_{3/2}$, 164.4 eV for S $2p_{1/2}$) and C-SO_x-C (167.8 eV) species (the inset in Fig. 3C).

The ORR catalytic performances of different carbon catalysts were first comparatively investigated in O_2-saturated alkaline solution. A series of linear sweep voltammograms (LSVs) were collected on a rotating disk electrode (RDE) at 1600 rpm (Fig. 3A). Remarkably, the N, S-CN exhibits a high ORR onset potential of -0.05 V vs. Ag/AgCl, which is much more positive than that of N-CN and RGO (-0.15 V and -0.16 V, respectively). The half-wave potential ($E_{1/2}$) of N, S-CN is -0.20V, and much closer to that of Pt/C (-0.15 V). Moreover, the unique and wide current plateau from -0.3 to -0.8 V observed on the N, S-CN represents a diffusion-controlled process corresponding to the efficient four-electron-dominated ORR pathway [18]. As for control materials, GDS shows negligible ORR catalytic activity (Fig. S6), and N-CN and RGO have apparently worse activities than that of N, S-CN. The most positive onset potential and half-wave potential on N, S-CN comparing with these counterparts suggest that this material has clearly best catalytic performance, which is most likely due to its large surface areas, unique mesoporous structure and more accessible catalytic active sites. Tafel slopes were then obtained from the polarization curves to investigate the difference in ORR catalytic kinetics on these non-metallic catalysts. As shown in Fig. 3B, N, S-CN exhibits a Tafel slope of 89 mV dec^{-1}, much lower than that of N-CN (141 mV dec^{-1}) and RGO (172 mV dec^{-1}) and close to that of Pt/C (65 mV dec^{-1}), suggesting the favourable ORR kinetics of the N, S-CN catalyst. It should be noted that the ORR performance of N, S-CN, especially the very positive half-wave potential, greatly surpasses those of previously reported graphitic C_3N_4 , dual-doped graphene materials including B, N-graphene and N, S-graphene [13,16,18], and non-noble metal hybridized eletrocatalysts such as Fe_3O_4/N-graphene, Mn_3O_4/N-graphene and CoO/carbon nanotube [49-51].

More detailed LSV studies at different rotating speeds (0-2400 rpm, Fig. S7) were carried out to quantitatively understand the ORR activities of these materials. The Koutecky-Levich (K-L) plots (J^{-1}vs $\omega^{-1/2}$) were calculated from LSVs and compared at different potentials. Noticeably, all K-L plots of N, S-CN display good linearity, and the N, S-CN shows a much higher ORR current density than that of N-CN at -0.6V. Furthermore, electron transfer numbers (n) and kinetic limiting current density (J_K) are calculated from the slopes and the intercepts of linear K-L plots on the basis of the K-L equation (Fig. 3C). N, S-CN shows a larger n value of 3.98 at -0.6 V than that of N-CN (3.52), suggesting its perfect selectivity for the efficient four-electron-dominated ORR pathway. Significantly, N, S-CN also shows the high J_K value of 16.0 mA cm^{-2} at -0.6 V, as compared to that of N-CN (6.5 mA cm^{-2}). Apparently, the large n and high J_K of N, S-CN are extremely close to those of Pt/C (n, ~4.00; J_K, ~16.3 mA cm^{-2}), further confirming its superior ORR performance. Moreover, N, S-CN shows stable and large n (3.89-4.0), and high J_K (13.6-16.5 mA cm^{-2}) over the potential range from -0.4 to -0.8 V, implying a smooth and electrochemically stable ORR process over the N, S-CN. The rotating ring-disk electrode (RRDE) technique was further employed to quantify materials' ORR efficiency (Fig. S8). Remarkably, the ORR on the N, S-CN yields about 2.0-3.8 % H_2O_2 over the potential range from -0.2 to -0.8 V with the n ranging from 3.92 to 3.96. For the N-CN, its n ranges from 3.0 to 3.4, and gives much higher amount of H_2O_2 (~29.7-48.9 %) under identical conditions. These results further indicate the superior ORR electrocatalytic efficiency of N, S-CN.

The electrocatalytic OER activity of different synthesized carbon catalysts was also evaluated in O_2-saturated 0.1 M KOH solution (Fig. 3D). For comparison purpose, the IrO_2-carbon nanotube composite (IrO_2-CNT) was prepared according to our previous work [52], because IrO_2 is commonly used as a reference to compare OER performance [53]. The current density of N, S-CN reaches 5 mA cm^{-2} at a potential of 0.65 V, which is higher than the 0.58 V for IrO_2-CNT but more negative than 0.76 V for N-CN. The operating potentials to deliver a 10 mA cm^{-2} current density ($E_{j=10}$) were then compared for different samples, which is the value expected for a 10% efficient solar water-

splitting device. The N, S-CN generates a current density of 10 mA cm^{-2} at 0.68 V, which is higher than that of IrO_2-CNT (0.62 V), but lower than those of the previously reported carbon-based catalysts including N, O-doped carbon hydrogels [20] and N-doped carbon nanocables [8], and comparable to those of metal-containing eletrocatalysts such as $Mn_3O_4/CoSe_2$ hybrids [54], Co_3O_4/N-graphene [55] and Mn_xO_y/N-doped carbon [9].

The catalytic kinetics for oxygen evolution was examined by Tafel plots (Fig. 3E). The Tafel slope of N, S-CN (53 mV dec^{-1}) is much lower than those of IrO_2-CNT (81 mV dec^{-1}) and N-CN (98 mV dec^{-1}). Compared with previously reported OER catalysts, the Tafel slope of N, S-CN is much lower than those of N, O-doped carbon hydrogels (141 mV dec^{-1}) [20], C_3N_4/carbon nanotube composites (83 mV dec^{-1}) [52] and most metal oxide OER catalysts including Co_3O_4/carbon nanowires (70 mV dec^{-1}) [56], CoO/N-graphene (71 mV dec^{-1}) [10] and Co_3O_4/N-graphene (67 mV dec^{-1}) [55], suggesting its extremely favorable reaction kinetics. The electrochemical impedance spectrum (EIS) can reflect the catalytic kinetics of different materials. As shown in Fig. 3F, N, S-CN has a low charge transfer resistance (~22 Ω) compared to those of N-CN, corresponding to its much more favorable charge transport kinetics.

The overall oxygen electrode activity has been evaluated by the difference of OER and ORR metrics ($\Delta E = E_{j=10} - E_{1/2}$) [57]. The smaller ΔE is, the closer the catalyst is to an ideal reversible oxygen electrode. Remarkably, the N, S-CN exhibits a ΔE of 0.88 V (Fig. 4A), which is much lower than that of most non-metallic materials (e.g. N, P-carbon paper, ΔE=0.96; N-graphene/CNT, ΔE=1.00 V) [57,58], also outperforms some highly active metal electrocatalysts including noble-metals (e.g. Pt/C, ΔE=0.94 V; Ir/C, ΔE=0.92 V) [9,59] and transition-metals (e.g. $CaMn_4O_x$, ΔE=1.04 V; Mn_xO_y/N-carbon, ΔE=0.93 V) [9,59]. The inset in Fig. 4A and Table S2 summarize a detailed comparison of different state-of-the-art bifunctional catalysts reported recently, further confirming the superior catalytic activity of the N, S-CN for both ORR and OER.

The stability of N, S-CN as a bifunctional ORR and OER catalyst was assessed through the chronoamperometric measurement. As shown in Fig. 4B, the N, S-CN exhibits a high ORR stability under a constant cathodic voltage of -0.5 V with maintaining a very slow attenuation over 40 h. The N, S-CN still retains 92.5 % of the initial current, whereas Pt/C shows nearly 40 % loss of its initial current over the same time period, confirming the better ORR stability of N, S-CN's active reaction sites than commercial Pt/C in alkaline environment. The CVs also reveal the reliable cyclic stability of the N, S-CN with almost no change during 1000 continuous potential cycles. Additionally, the methanol crossover effect was also evaluated (the inset in Fig. 4B, and Fig. S9). After adding 3 M methanol to the electrolyte, the CV curve and original cathodic ORR current of N, S-CN remain almost unchanged, whereas the corresponding current on Pt/C instantaneously shifts from a cathodic ORR current to a reversed anodic current owing to the methanol oxidation reaction on Pt/C [60,61]. The OER chronoamperometric curve of N, S-CN (Fig. 4C) shows an insignificant anodic current attenuation of 4.7 % within 3 h. Furthermore, 90.3 % of the original catalytic current can be retained after 200 continuous potential cycles (the inset of Fig. 4C). The remarkable electrochemical stability and excellent catalytic selectivity of the N, S-CN make it highly promising as an superior bifunctional oxygen electrocatalyst.

On the basis of structure-property relationship, the outstanding bifunctional ORR and OER activity of N, S-CN should originate from its multiple doping, unique porous architecture and excellent charge-transfer ability. First, N, S-CN contains 4.1 at.% N, 6.1 at.% S and 15.2 at.% O and thus affords high concentrations of active sites. The electron-accepting N species can impart a relatively high positive charge density on neighboring sp^2-bonded C atoms [13,52], while the S atoms are positively charged because of the mismatch of outermost orbitals of S and C. Hence, both of them can be viewed as the catalytic centers [22,23]. On the other hand, the codoping of S and N gives rise to asymmetrical spin and charge density, and thus generates synergistic effects which can substantially increase the number of active C atoms and significantly elevate ORR and OER catalytic

activity [16]. In addition, significant amount of O species can render the catalyst highly hydrophilic for more accessible catalytic surfaces, and consequently expedite catalytic processes [20,25]. Secondly, nitrogen adsorption has confirmed the N, S-CN has the unique mesoporous structure together with a large active surface area, which can also be evaluated by the electrochemical double-layer capacitance (C_{dl}). As shown in Fig. S10, the C_{dl} of N, S-CN is confirmed to be 11.1 mF cm^{-2}, much higher than that of N-CN (3.2 mF cm^{-2}). Since C_{dl} is proportional to the active surface area of electrocatalysts, better exposure and enhanced utilization of electroactive sites on the large active surface of N, S-CN greatly contribute to its efficient ORR and OER activities [62]. Besides the in-plane mesoporous structure, the existence of abundant crinkles on the surface of carbon nanosheets also facilitates the formation of large interlayer pores (Fig. S2), which can provide a smooth pathway for the facile transportation of reactants and products associated with the electrochemical reactions (the access of O_2 in ORR and the release of O_2 in OER) [20,63,64]. Thirdly, the excellent charge-transfer ability is imperative for a good electrocatalyst. Graphene oxide substrate can transform to highly conductive reduced graphene oxide after pyrolysis. The more exposure of graphene surface due to the mesoporous structure of N, S-CN further improves its overall charge-tranfer capability, which has been evidenced by the EIS study. On the other hand, the unique adhesive capability of PDA endows the two-component (graphene and PDA) integrated carbon nanosheets with the mutually strong coupling and excellent structural stability, which not only facilitates the charge transfer between these two components, but also provides a guarantee for the long-term durability in electrochemical tests.

Conclusion

In summary, a robust, highly efficient and environmentally benign method has been developed to introduce S to the GO-PDA hybrids to produce N, S-codoped mesoporous carbon nanosheets. As a result, the fabricated mesoporous carbon nanosheets have exhibited much better performances than

most of other benchmarked bifunctional ORR and OER catalysts, which are attributed to their multiple doping, unique porous architecture and excellent charge-transfer ability. Due to the versatile physicochemical properties and tunable nanostructures of PDA, this work provides a universal platform towards the design and construction of heteroatom doped carbons and metal-N decorated carbon materials, which would be highly promising for the next generation of fuel cells, metal air batteries and photocatalysis applications.

Acknowledgements

This work was financially supported by the Australian Research Council (ARC) through the Discovery Projects of DP110102877, DP130104459 and DP140104062.

Appendix A. Supplementary materials

Supplementary data associated with this article can be found in the online version at http://dx.doi.org/xxxx.

References

[1] M. Armand, J.M. Tarascon, Nature 451 (2008) 652-657.

[2] B.C.H. Steele, A. Heinzel, Nature 414 (2001) 345-352.

[3] Y.-C. Lu, Z. Xu, H.A. Gasteiger, S. Chen, K. Hamad-Schifferli, Y. Shao-Horn, J. Am. Chem. Soc. 132 (2010) 12170-12171.

[4] T. Reier, M. Oezaslan, P. Strasser, ACS Catalysis 2 (2012) 1765-1772.

[5] I. Katsounaros, S. Cherevko, A.R. Zeradjanin, K.J.J. Mayrhofer, Angew. Chem. Int. Ed. 53 (2014) 102-121.

[6] F.D. Kong, S. Zhang, G.P. Yin, Z.B. Wang, C.Y. Du, G.Y. Chen, N. Zhang, Int. J. Hydrogen Energy 37 (2011) 59-67.

[7] F. Cheng, J. Shen, B. Peng, Y. Pan, Z. Tao, J. Chen, Nat. Chem. 3 (2011) 79-84.

[8] G.-L. Tian, Q. Zhang, B. Zhang, Y.-G. Jin, J.-Q. Huang, D.S. Su, F. Wei, Adv. Funct. Mater. 24 (2014) 5956-5961.

[9] J. Masa, W. Xia, I. Sinev, A. Zhao, Z. Sun, S. Grützke, P. Weide, M. Muhler, W. Schuhmann, Angew. Chem. Int. Ed. 53 (2014) 8508-8512.

[10] S. Mao, Z. Wen, T. Huang, Y. Hou, J. Chen, Energy Environ. Sci. 7 (2014) 609-616.

[11] K. Gong, F. Du, Z. Xia, M. Durstock, L. Dai, Science 323 (2009) 760-764.

[12] Y. Tang, B.L. Allen, D.R. Kauffman, A. Star, J. Am. Chem. Soc. 131 (2009) 13200-13201.

[13] Y. Zheng, Y. Jiao, J. Chen, J. Liu, J. Liang, A. Du, W. Zhang, Z. Zhu, S.C. Smith, M. Jaroniec, G.Q. Lu, S.Z. Qiao, J. Am. Chem. Soc. 133 (2011) 20116-20119.

[14] Y. Jiao, Y. Zheng, M. Jaroniec, S.Z. Qiao, J. Am. Chem. Soc. 136 (2014) 4394-4403.

[15] S. Chen, J. Duan, M. Jaroniec, S.Z. Qiao, Angew. Chem. Int. Ed. 52 (2013) 13567-13570.

[16] J. Liang, Y. Jiao, M. Jaroniec, S.Z. Qiao, Angew. Chem. Int. Ed. 51 (2012) 11496-11500.

[17] Y. Meng, D. Voiry, A. Goswami, X. Zou, X. Huang, M. Chhowalla, Z. Liu, T. Asefa, J. Am. Chem. Soc. 136 (2014) 13554-13557.

[18] Y. Zheng, Y. Jiao, L. Ge, M. Jaroniec, S.Z. Qiao, Angew. Chem. 125 (2013) 3192-3198.

[19] L. Wang, P. Yu, L. Zhao, C. Tian, D. Zhao, W. Zhou, J. Yin, R. Wang, H. Fu, Sci. Rep. 4 (2014) 5184.

[20] S. Chen, J. Duan, M. Jaroniec, S.-Z. Qiao, Adv. Mater. 26 (2014) 2925-2930.

[21] H.L. Poh, P. Šimek, Z. Sofer, M. Pumera, ACS Nano 7 (2013) 5262-5272.

[22] Z. Yang, Z. Yao, G. Li, G. Fang, H. Nie, Z. Liu, X. Zhou, X.a. Chen, S. Huang, ACS Nano 6 (2011) 205-211.

[23] S. Yang, L. Zhi, K. Tang, X. Feng, J. Maier, K. Müllen, Adv. Funct. Mater. 22 (2012) 3634-3640.

[24] Y. Ito, W. Cong, T. Fujita, Z. Tang, M. Chen, Angew. Chem. Int. Ed. 54 (2015) 2131-2136.

[25] R. Silva, D. Voiry, M. Chhowalla, T. Asefa, J. Am. Chem. Soc. 135 (2013) 7823-7826.

[26] S.-A. Wohlgemuth, R.J. White, M.-G. Willinger, M.-M. Titirici, M. Antonietti, Green Chem. 14 (2012) 1515-1523.

[27] K. Qu, Y. Zheng, S. Dai, S.Z. Qiao, Nanoscale 7 (2015) 12598-12605.

[28] N. Gavrilov, I.A. Pašti, M. Mitrić, J. Travas-Sejdić, G. Ćirić-Marjanović, S.V. Mentus, J. Power Sources 220 (2012) 306-316.

[29] R. Liu, S.M. Mahurin, C. Li, R.R. Unocic, J.C. Idrobo, H. Gao, S.J. Pennycook, S. Dai, Angew. Chem. Int. Ed. 50 (2011) 6799-6802.

[30] X. Yu, H. Fan, L. Wang, Z. Jin, Angew. Chem. Int. Ed. 53 (2014) 12600-12604.

[31] R. Li, K. Parvez, F. Hinkel, X. Feng, K. Müllen, Angew. Chem. Int. Ed. 52 (2013) 5535-5538.

[32] K.-Y. Ju, Y. Lee, S. Lee, S.B. Park, J.-K. Lee, Biomacromolecules 12 (2011) 625-632.

[33] C. Xu, K. Xu, H. Gu, R. Zheng, H. Liu, X. Zhang, Z. Guo, B. Xu, J. Am. Chem. Soc. 126 (2004) 9938-9939.

[34] M.J. LaVoie, B.L. Ostaszewski, A. Weihofen, M.G. Schlossmacher, D.J. Selkoe, Nat. Med. 11 (2005) 1214-1221.

[35] H. Lee, S.M. Dellatore, W.M. Miller, P.B. Messersmith, Science 318 (2007) 426-430.

[36] L.Q. Xu, W.J. Yang, K.-G. Neoh, E.-T. Kang, G.D. Fu, Macromolecules 43 (2010) 8336-8339.

[37] N.F. Della Vecchia, R. Avolio, M. Alfè, M.E. Errico, A. Napolitano, M. d'Ischia, Adv. Funct. Mater. 23 (2013) 1331-1340.

[38] C.J. Cooksey, E.J. Land, F.A.P. Rushton, C.A. Ramsden, P.A. Riley, Quant. Struct.-Act. Relat. 15 (1996) 498-503.

[39] M.-H. Ryou, J. Kim, I. Lee, S. Kim, Y.K. Jeong, S. Hong, J.H. Ryu, T.-S. Kim, J.-K. Park, H. Lee, J.W. Choi, Adv. Mater. 25 (2013) 1571-1576.

[40] H. Jiang, L. Yang, C. Li, C. Yan, P.S. Lee, J. Ma, Energy Environ. Sci. 4 (2011) 1813-1819.

[41] K. Ai, Y. Liu, C. Ruan, L. Lu, G. Lu, Adv. Mater. 25 (2013) 998-1003.

[42] Y.M. Yu, J.H. Zhang, C.H. Xiao, J.D. Zhong, X.H. Zhang, J.H. Chen, Fuel Cells 12 (2012) 506-510.

[43] D.C. Marcano, D.V. Kosynkin, J.M. Berlin, A. Sinitskii, Z. Sun, A. Slesarev, L.B. Alemany, W. Lu, J.M. Tour, ACS Nano 4 (2010) 4806-4814.

[44] M. d'Ischia, A. Napolitano, A. Pezzella, P. Meredith, T. Sarna, Angew. Chem. Int. Ed. 48 (2009) 3914-3921.

[45] S. Hong, Y.S. Na, S. Choi, I.T. Song, W.Y. Kim, H. Lee, Adv. Funct. Mater. 22 (2012) 4711-4717.

[46] A.C. Ferrari, J.C. Meyer, V. Scardaci, C. Casiraghi, M. Lazzeri, F. Mauri, S. Piscanec, D. Jiang, K.S. Novoselov, S. Roth, A.K. Geim, Phys. Rev. Lett. 97 (2006) 187401.

[47] S.M. Kang, S. Park, D. Kim, S.Y. Park, R.S. Ruoff, H. Lee, Adv. Funct. Mater. 21 (2011) 108-112.

[48] K. Qu, J. Wang, J. Ren, X. Qu, Chem. Eur. J. 19 (2013) 7243-7249.

[49] Y. Liang, H. Wang, P. Diao, W. Chang, G. Hong, Y. Li, M. Gong, L. Xie, J. Zhou, J. Wang, T.Z. Regier, F. Wei, H. Dai, J. Am. Chem. Soc. 134 (2012) 15849-15857.

[50] Z.-S. Wu, S. Yang, Y. Sun, K. Parvez, X. Feng, K. Müllen, J. Am. Chem. Soc. 134 (2012) 9082-9085.

[51] J. Duan, S. Chen, S. Dai, S.Z. Qiao, Adv. Funct. Mater. 24 (2014) 2072-2078.

[52] T.Y. Ma, S. Dai, M. Jaroniec, S.Z. Qiao, Angew. Chem. Int. Ed. 53 (2014) 7281-7285.

[53] Q. Zhu, L. Lin, Y.-F. Jiang, X. Xie, C.-Z. Yuan, A.-W. Xu, New J. Chem. 39 (2015) 6289-6296.

[54] M.-R. Gao, Y.-F. Xu, J. Jiang, Y.-R. Zheng, S.-H. Yu, J. Am. Chem. Soc. 134 (2012) 2930-2933.

[55] Y. Liang, Y. Li, H. Wang, J. Zhou, J. Wang, T. Regier, H. Dai, Nat. Mater. 10 (2011) 780-786.

[56] T.Y. Ma, S. Dai, M. Jaroniec, S.Z. Qiao, J. Am. Chem. Soc. 136 (2014) 13925-13931.

[57] T.Y. Ma, J. Ran, S. Dai, M. Jaroniec, S.Z. Qiao, Angew. Chem. Int. Ed. 54 (2015) 4646-4650.

[58] G.-L. Tian, M.-Q. Zhao, D. Yu, X.-Y. Kong, J.-Q. Huang, Q. Zhang, F. Wei, Small 10 (2014) 2251-2259.

[59] Y. Gorlin, T.F. Jaramillo, J. Am. Chem. Soc. 132 (2010) 13612-13614.

[60] L. Wang, J. Yin, L. Zhao, C. Tian, P. Yu, J. Wang, H. Fu, Chem. Commun. 49 (2013) 3022-3024.

[61] L. Zhao, L. Wang, P. Yu, D. Zhao, C. Tian, H. Feng, J. Ma, H. Fu, Chem. Commun. 51 (2015) 12399-12402.

[62] J. Zhang, Z. Zhao, Z. Xia, L. Dai, Nat. Nanotech. 10 (2015) 444-452.

[63] S. Chen, S.-Z. Qiao, ACS Nano 7 (2013) 10190-10196.

[64] S. Chen, J. Duan, J. Ran, M. Jaroniec, S.Z. Qiao, Energy Environ. Sci. 6 (2013) 3693-3699.

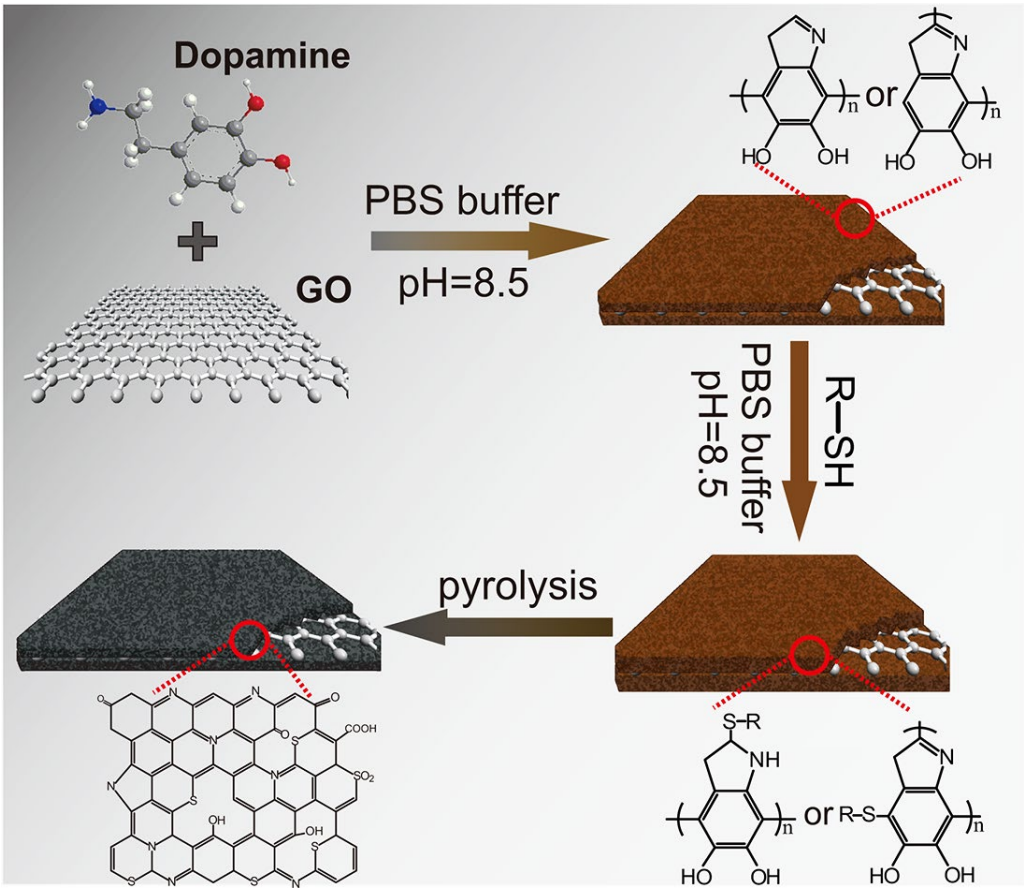

Scheme 1 Fabrication of GDS derived carbon nanosheets (N, S-CNs), where R-SH refers to 2-mercaptoethanol.

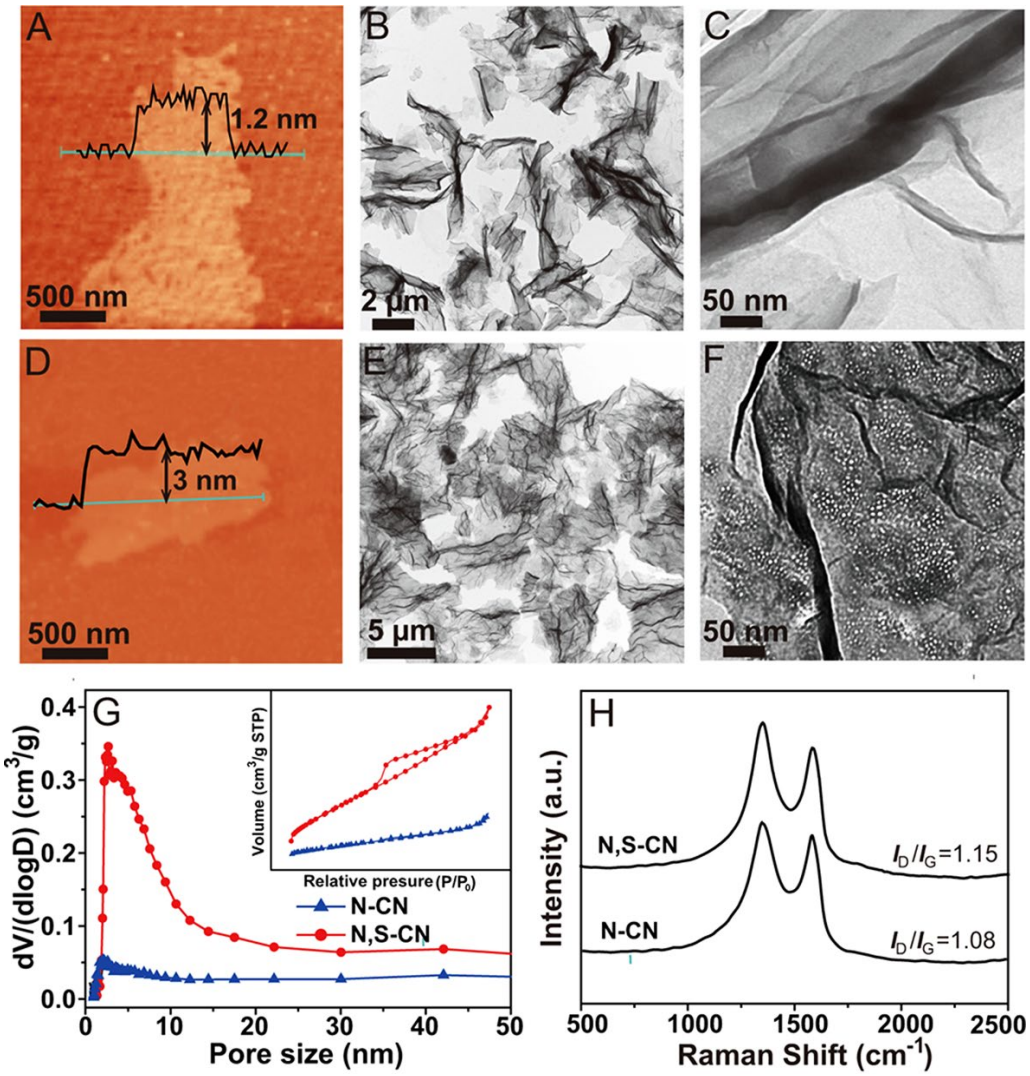

Fig. 1 (A) AFM and (B, C) TEM images of N-CN. (D) AFM and (E, F) TEM images of N, S-CN. (G) The pore size distribution curves of N-CN and N, S-CN; the inset shows the corresponding nitrogen adsorption-desorption isotherms. (H) Raman spectra of N-CN and N, S-CN.

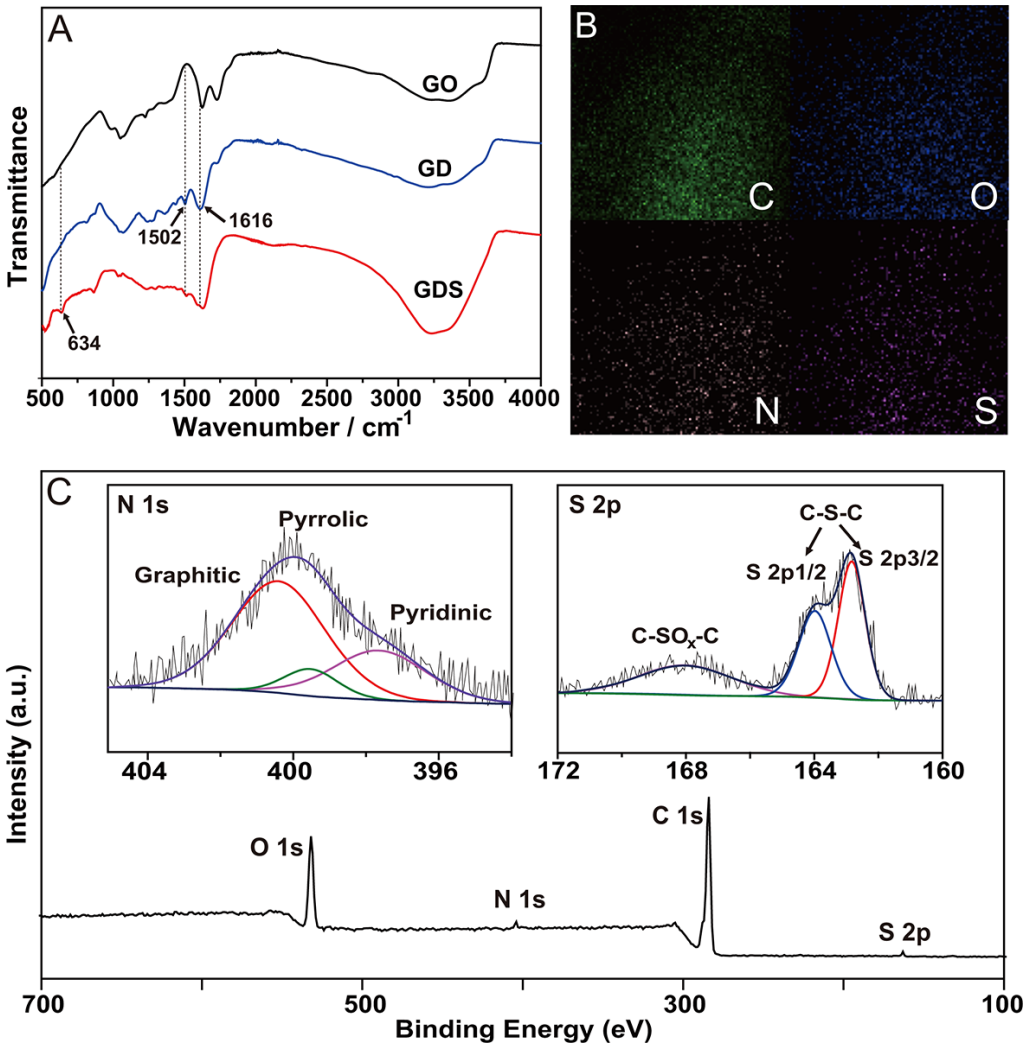

Fig. 2 (A) FTIR spectra of GO, GD and GDS. (B) TEM elemental mapping of C, O, N and S in N, S-CN. (C) XPS spectra: N 1s, S 2p, and survey of N, S-CN.

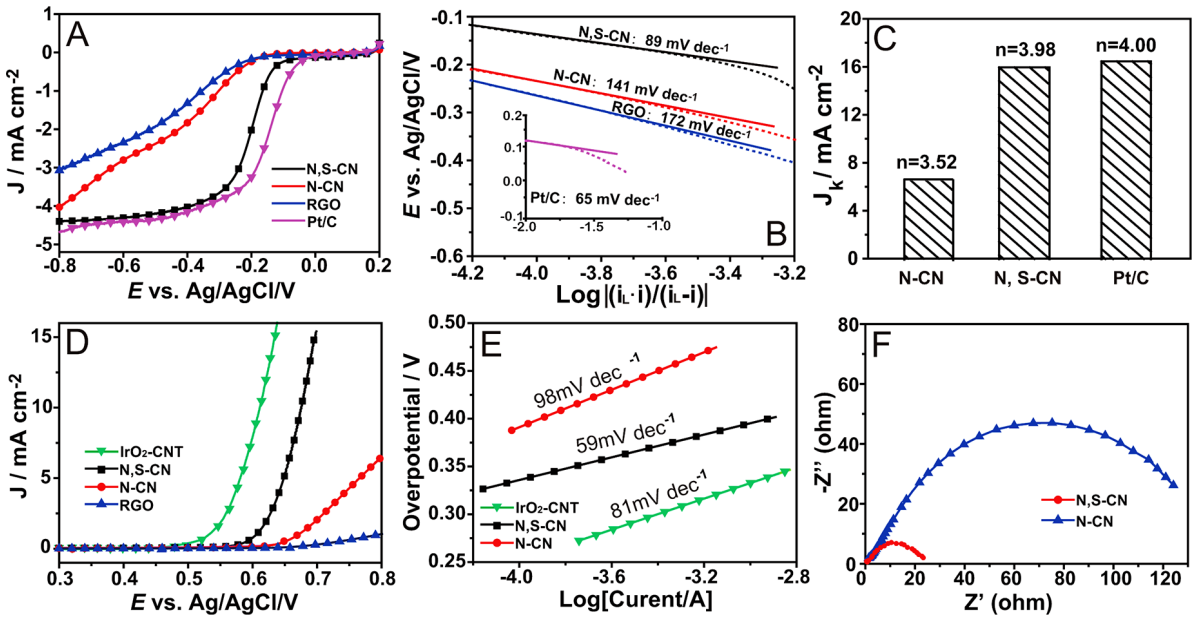

Fig. 3 (A) ORR LSVs at a sweep rate of 5 mV s^{-1}. (B) ORR Tafel slope obtained from the LSVs at 1600 rpm, (Inset: Tafel slope of Pt/C). (C) kinetic limiting current density (J_k) and electron transfer number (n) of N-CN, N, S-CN and Pt/C. (D) OER LSVs at a sweep rate of 5 mV s^{-1}. (E) OER Tafel plots. (F) The electrochemical impedance spectra (recorded at 0.65 V) of N-CN and N, S-CN.

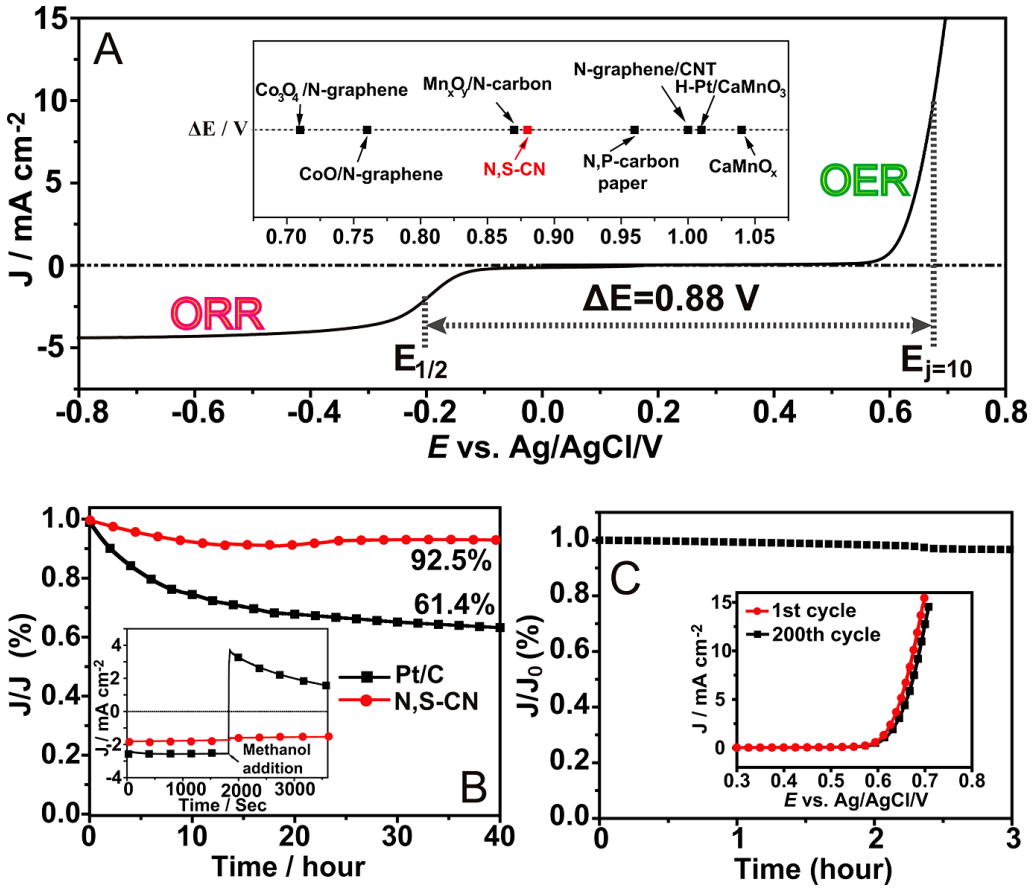

Fig. 4 (A) The overall LSV curve of N, S-CN in the potential range of -0.8-0.8 V, ΔE ($E_{j=10}$—$E_{1/2}$) is a metric for bifunctional ORR and OER activity (Inset: the value of ΔE for various catalysts reported previously). (B) ORR current-time chronoamperometric response of N, S-CN and Pt/C in O_2-saturated 0.1 M KOH solution (Inset: current-time chronoamperometric response of N, S-CN and Pt/C before and after addition of 3 M methanol). (C) OER current-time chronoamperometric response of N, S-CN at 0.65 V in O_2-saturated 0.1 M KOH solution (Inset : the LSV plots in the beginning and after 200 cycles).

Table of contents:

N, S-codoped mesoporous carbon nanosheets are facilely derived from the graphene oxide-polydopamine hybrids through a novel, highly efficient and environmentally benign method. The optimized material can act as the superior bifunctional electrocatalysts for oxygen reduction and oxygen evolution, and its performances are even better than transition-metal and noble metal catalysts because of its high concentration of multiple dopants, abundant porous architecture and excellent charge-transfer ability.

Keyword: mesoporous carbon nanosheets, nonmetallic co-doping, oxygen reduction, oxygen evolution, bifunctional, electrocatalysis.

Konggang Qu, Yao Zheng, Sheng Dai, and Shi Zhang Qiao.

Title: Grpahene Oxide-Polydopamine Derived N, S-codoped Carbon Nanosheets as Superior Bifunctional Electrocatalysts for Oxygen Reduction and Evolution

ToC Fig.:

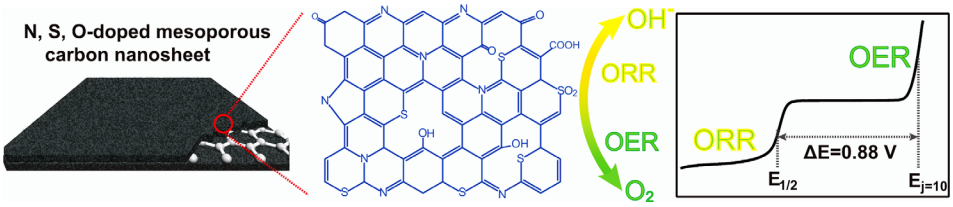

Supplementary materials

Graphene Oxide-Polydopamine Derived N, S-codoped Carbon Nanosheets as Superior Bifunctional Electrocatalysts for Oxygen Reduction and Evolution

Konggang Qu, Yao Zheng, Sheng Dai and Shi Zhang Qiao

School of Chemical Engineering, The University of Adelaide, Adelaide, SA, 5005, Australia

Preparation of Graphene Oxide (GO)

Graphite flakes were oxidized using the improved Hummers' method. Graphite (3 g) was added into a mixture of concentrated H_2SO_4/H_3PO_4 (360:40 mL), followed by the addition of $KMnO_4$ (18 g). The reaction mixture was heated to 50 ºC and stirred for 12 hours. The reaction was then cooled to room temperature and poured into ice water (ca. 400 mL) with addition of H_2O_2 (30 %, 20 mL). The mixture was then filtered over a 0.45 µm PTFE membrane and washed with 200 mL of water, 200 mL of 30 % HCl, and 200 mL of ethanol (2×) to obtain graphite oxide.

Exfoliation of the above prepared graphite oxide to graphene oxide (GO) was achieved by ultrasonication of the diluted graphite oxide dispersion using a Brandson Digital Sonifier (S450D, 500 W, 30 % amplitude) for 30 min. The resulting brownish dispersion was subjected to 20 min of centrifugation at 3000 rpm to remove any unexfoliated graphite oxide. The GO powder was collected by lyophilization for further characterization and modificaton.

Electrochemical measurements

Cyclic voltammogram (CV), linear sweep voltammogram (LSV), and rotating disk electrode (RDE) tests were carried out using a glassy carbon rotating disk electrode. The scan rate of CVs was kept as 50 mV s^{-1} while that for LSVs and RDE tests was 5 mV s^{-1}.

For ORR, the Koutecky-Levich plots were obtained by linear fitting of the reciprocal rotating speedversus reciprocal current density collected at different potentials form -0.4 V to -0.8 V. The overall electron transfer numbers per oxygen molecule involved in a typical ORR process were calculatedfrom the slopes of Koutecky-Levich plots using the following equation:

$$1/j_D=1/j_k + 1/ B\omega^{1/2} \qquad (1)$$

where j_k is the kinetic current in amperes at a constant potential, ω is the electrode rotating speed in rpm, and B is the reciprocal of the slope determined from Koutecky-Levich plots based on Levich Equation:

$$B=0.2\ nFA\nu^{-1/6}C_{O2}D_{O2}^{2/3} \qquad (2)$$

where n is the number of electrons transferred per oxygen molecule, F is the Faraday constant (96485 C mol^{-1}), D_{O2} is the diffusion coefficient of O_2 in 0.1 M KOH (1.9×10^{-5} cm s^{-1}), ν is the kinetic viscosity, and C_{O2} is the concentration of O_2 (1.2×10^{-3} mol L^{-1}). The constant 0.2 is adopted when the rotating speed is in rpm.

Rotating ring-disk electrode (RRDE) voltammogram measurements were conducted on an RRDE configuration with a 320 μm gap Pt ring electrode. The linear sweep voltammograms were recorded in O_2 saturated 0.1 M KOH at 1600 rpm. The disk was set to scan at 5 mV s^{-1} from 0.2 to -0.8 V and the ring was set at 0.5 V. The collecting efficiency of RRDE (N) was 0.37. The peroxide yield (HO_2^- %) and the electron transfer number (n) were calculated as follows:

$$HO_2^-\%=200\times I_r/N/(I_d+I_r/N) \qquad (3)$$

$$n=4\times I_d/(I_d+I_r/N) \qquad (4)$$

where I_d is the disk current and I_r is the ring current.

For ORR, the materials' resistance to methanol crossover effect and stability were tested in the same setup as the RDE tests in O_2 saturated 0.1 M KOH aqueous electrolyte. The stability test was performed at a static potential of -0.3 V and -0.5 V, respectively, for the chronoamperometry at room temperature.

Electrochemical impedance spectroscopy (EIS) measurements were performed by applying an AC voltage with 5 mV amplitude in a frequency range from 100000 to 1 Hz and recorded at 0.65 V vs. Ag/AgCl. The electrochemical double layer capacitances (C_{dl}) of the as-synthesized materials were measured from double-layer charging curves using cyclic voltammograms (CVs) in a potential range of 0-0.05 V. Working electrodes were scanned for several potential cycles until the signals were stabilized, and then the CV data were collected. Then, the capacitive currents, i.e. $\Delta J_{|Ja-Jc|}$ @ 0.025 V, were plotted as a function of CV scan rate. Linear relationship was observed with the slope twice larger than the C_{dl} value.

For OER, materials' stability was tested in O_2 saturated 0.1 M KOH aqueous electrolyte and performed at a static potential of 0.65 V for the chronoamperometry at room temperature.

Table S1. Comparison on the recently reported methods for S-doping.

Final product	S-doping precursor	Doping method	Temperature and doping efficiency	Application	Reference
S-doped graphene	Benzyl disulfide (BDS)	High temperature pyrolysis	600 °C : 1.53% 900 °C : 1.35% 1050 °C : 1.30%	Oxygen reduction reaction	Acs Nano, 6, 205 (2012).
N,S-doped graphene	Benzyl disulfide (BDS)	High temperature pyrolysis	900 °C : 2.0%	Oxygen reduction reaction	Angew. Chem. Int., Ed. 51, 11496 (2012)
S-doped graphene	H_2S	High temperature pyrolysis	500-900 °C : 1.2%-1.7%	Oxygen reduction reaction	Adv. Funct. Mater., 22, 3634 (2012).
N, S-doped graphene	2-aminothiophenol	High temperature pyrolysis	650 °C : 0.86%	Li-ion batteries and oxygen reduction reaction	Adv. Mater., 26, 6186 (2014).
S-doped graphene(1)	SO_2, or H_2S	High temperature pyrolysis	H_2S, 600 °C : 0.75% SO_2, 600 °C : 0.87%	Oxygen reduction reaction	Acs Nano, 7, 5262 (2013).
S-doped graphene(2)	SO_2, H_2S, or CS_2	High temperature pyrolysis	H_2S, 600 °C : 4.44% SO_2, 600 °C : 2.13% SO_2, 1000 °C : 2.16% CS_2, 1000 °C : 4.07%	Oxygen reduction reaction	Acs Nano, 7, 5262 (2013).
S-doped graphene(3)	SO_2, H_2S, or CS_2	High temperature pyrolysis	H_2S, 600 °C : 7.03% SO_2, 600 °C : 6.67%	Oxygen reduction reaction	Acs Nano, 7, 5262 (2013).
N, S-doped nanoporous graphene	Thiophene gas	High temperature CVD	500 °C : 5.06% 800 °C : 0.56%	Hydrogen evolution reaction	Angew. Chem. Int. Ed., 54, 2131 (2015).
N, S-codoped mesoporous carbon nanosheet	2-mercaptoethanol	High temperature pyrolysis	700 °C : 6.72% 800 °C : 6.11% 900 °C : 3.92%	Oxygen reduction and oxygen evolution reaction	This work

Notes:
(1) Graphene oxide is synthesized by Staudenmaier' method.
(2) Graphene oxide is synthesized by Hofmann' method.
(3) Graphene oxide is synthesized by Hummers' method.

Table S2. Comparison on the electrocatalytic activity of the recently reported bifunctional ORR and OER catalysts.

Catalyst	ORR onset potential (V vs. RHE)	ORR Tafel slope (mV dec^{-1})	OER Tafel slope (mV dec^{-1})	OER potential @10mV cm^{-2} ($E_{j=10}$) (V vs. RHE)	Overall oxygen electrode activity ΔE ($E_{j=10} - E_{1/2}$) (V)	Catalsyt loading (mg cm^{-2})	electrolyte	Active species	Reference
N, P-carbon paper	0.94	122.3	61.6	1.63	0.96	~0.20	0.1 M KOH	N, P	Angew. Chem. Int. Ed., 54, 4646 (2015).
N-graphene/CNT	0.88	N.A.	83	1.63	1.00	0.2548	0.1 M KOH	N	Small, 10, 2251 (2014).
H-Pt/$CaMnO_3$	0.90	65	N.A.	1.80	1.01	0.085	0.1 M KOH	Pt	Adv. Mater., 26, 2047 (2014).
Mn_xO_y/N -carbon	0.85	N.A.	82.6	1.68	0.87	0.21	0.1 M KOH	Mn-N	Angew. Chem. Int. Ed., 53, 8508 (2014).
$CaMn_4O_x$	0.85	N.A.	N.A.	1.77	1.04	N.A.	0.1 M KOH	Mn	J. Am. Chem. Soc., 132, 13612 (2010).
CoO/N-graphene	0.90	48	71	1.57	0.76	0.7	1 M KOH	Co-N	Energy Environ. Sci., 7, 609 (2014).
Co_3O_4/N-graphene	0.86	37	67	1.54	0.71	1.0	1 M KOH	Co-N	Nat. Mater., 10, 780 (2011).
Cu-MOF/graphene oxide	0.29	69	65	1.59	N.A.	0.2263	0.5 M H_2SO_4	Cu	Adv. Funct. Mater., 23, 5363 (2013).
N, S, O-carbon nanosheet (1)	0.92	89	53	1.65	0.88	0.20	0.1 M KOH	N, S, O	This work

Notes:

(1) For the convenience of comparision, the measure potentials *vs.*Ag/AgCl were converted to a reversible hydrogen electrode (RHE) scale accorting to the Nerst equation ($E_{RHE} = E_{Ag/AgCl} + 0.059 \times pH + 0.205$).

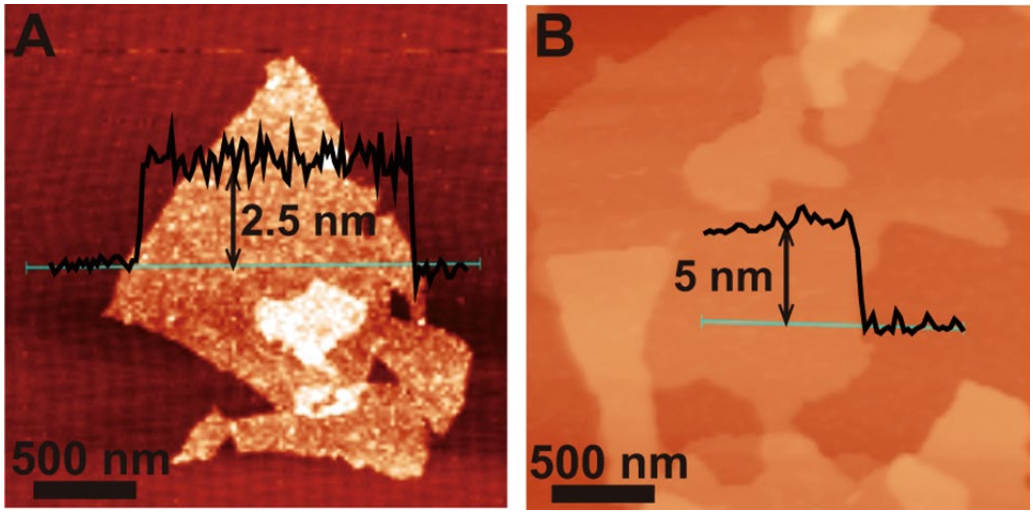

Figure S1. AFM images of GD and GDS.

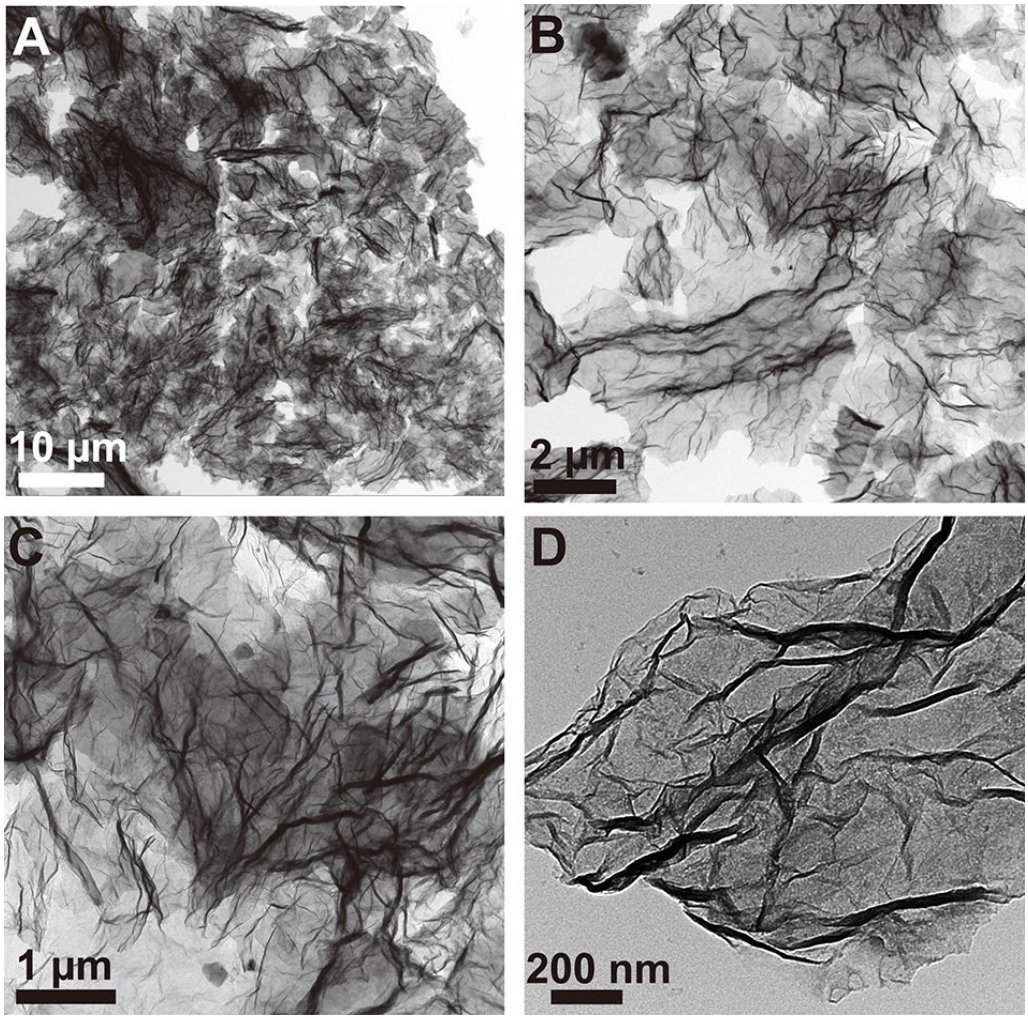

Figure S2. TEM images of N, S-CN at different magnifications.

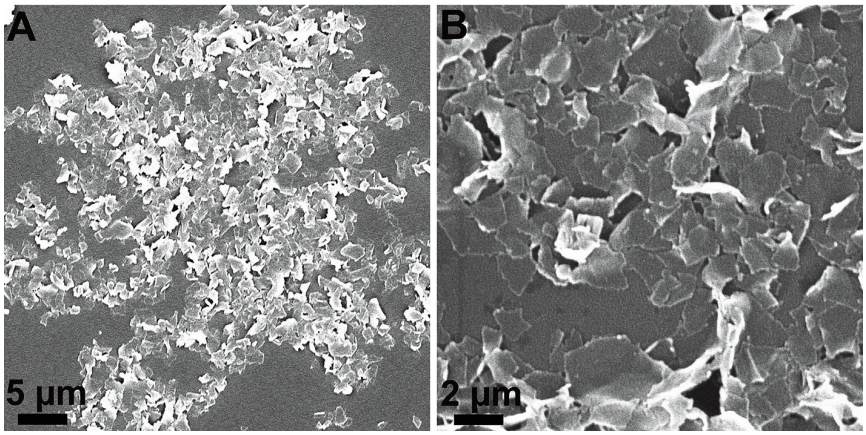

Figure S3. SEM images of the N, S-CN at different magnifications.

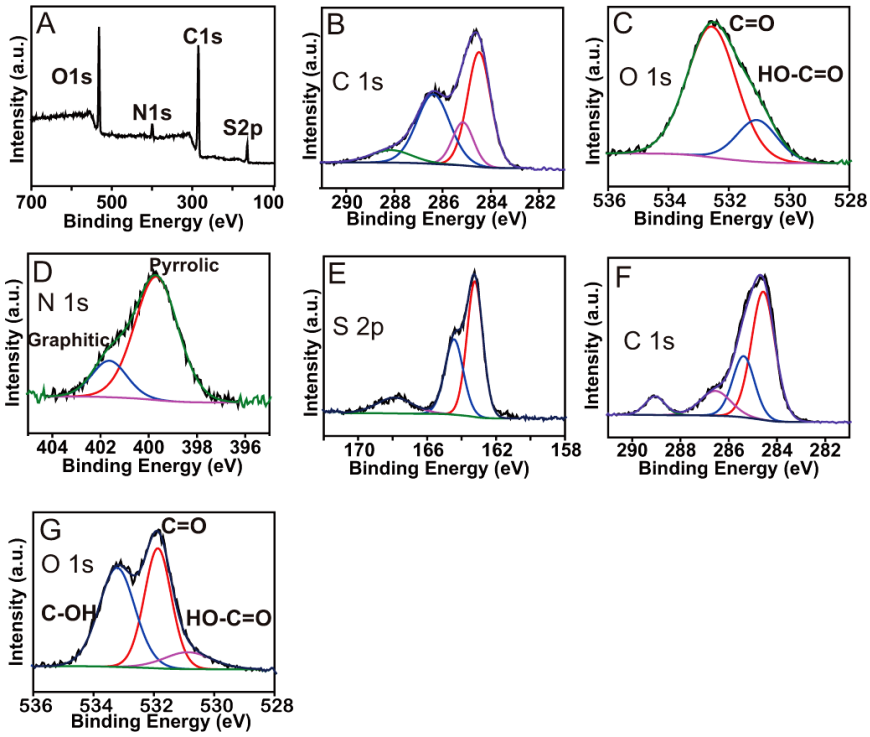

Figure S4. (A-E) XPS survey spectra, high-resolution spectra of C 1s, O 1s, N 1s and S 2p of GDS, (F, G) high-resolution spectra of C1s and O1s of N, S-CN.

For C1s spectra, the main peaks are deconvoluted into four peaks: 284.6 (C=C), 285.5 (C-N/C-S), 286.5 (C-O), and 289.0 eV (C=O/HO-C=O). For O1s spectra, the main peaks are deconvoluted into three peaks: 530.8 (HO-C=O), 532.1 (C=O) and 533.2 eV (C-OH). For N1s spectra, the main peaks are deconvoluted into three peaks: 398.0 (pyridinic), 399.7 (pyrrolic) and 400.8 (graphitic). For S2p spectra, the main peaks are deconvoluted into three peaks: 163.2 (C-S, $S2p_{3/2}$), 164.4 (C-S, $S2p_{1/2}$) and 167.8 eV (C-SO_x-C).

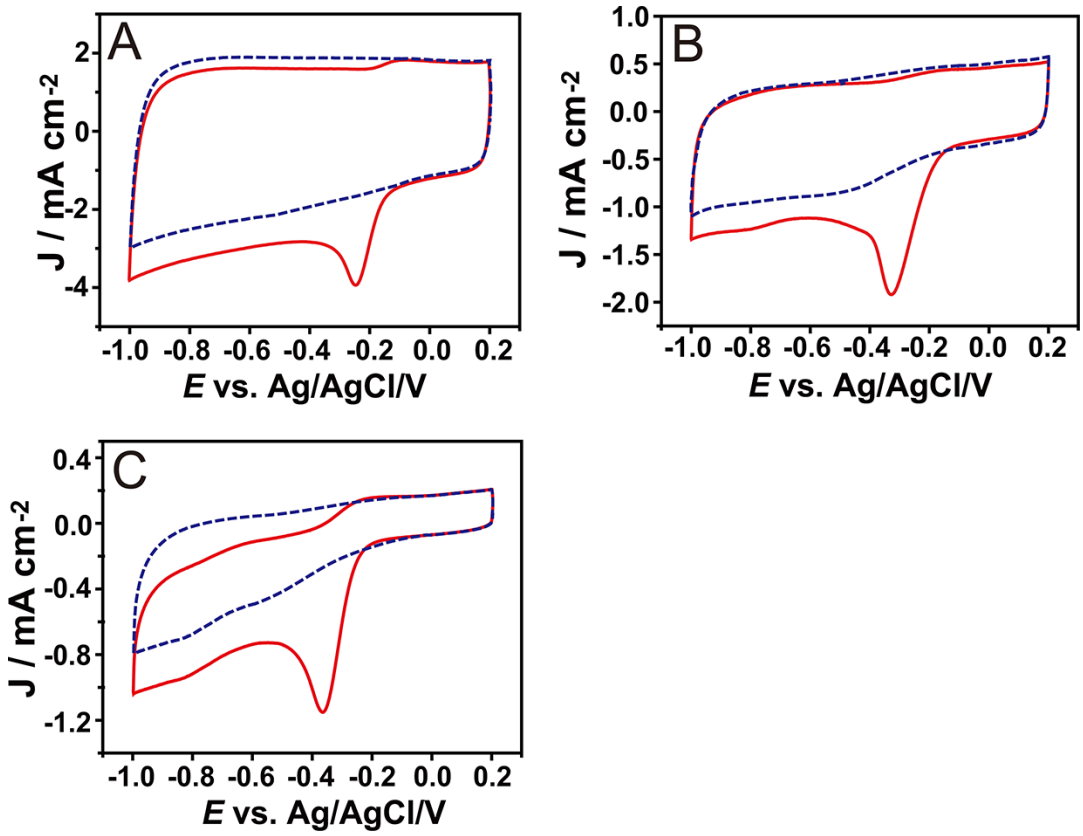

Figure S5. CV curves of A) N, S-CN, B) N-CN and C) RGO from 0.2 V to -1.0 V vs Ag/AgCl in N_2 or O_2 saturated 0.1 M KOH aqueous electrolyte. Scan rate is 100 mV s^{-1}.

As shown in **Figure S5**, the voltammogram of N, S-CN in N_2 saturated 0.1 M KOH electrolyte shows a quasi-rectangular shape without obvious redox peak in the potential range from -1.0 to 0.2 V, indicating the typical supercapacitance effect on porous carbon materials. In contrast, a well-defined cathodic peak centered at -0.24 V with a reaction current of -3.9 mA cm^{-2} appears in the CV when O_2 was introduced. The ORR reaction current of N, S-CN is much higher than that of N-CN (-1.9 mA cm^{-2}) or RGO (-1.2 mA cm^{-2}). Moreover, the peak potential for N-S-G is more positive than that of N-CN (-0.34 V) and RGO (-0.38 V), suggesting more efficient electrocatalytic activity of the as-prepared N, S-CN for oxygen reduction.

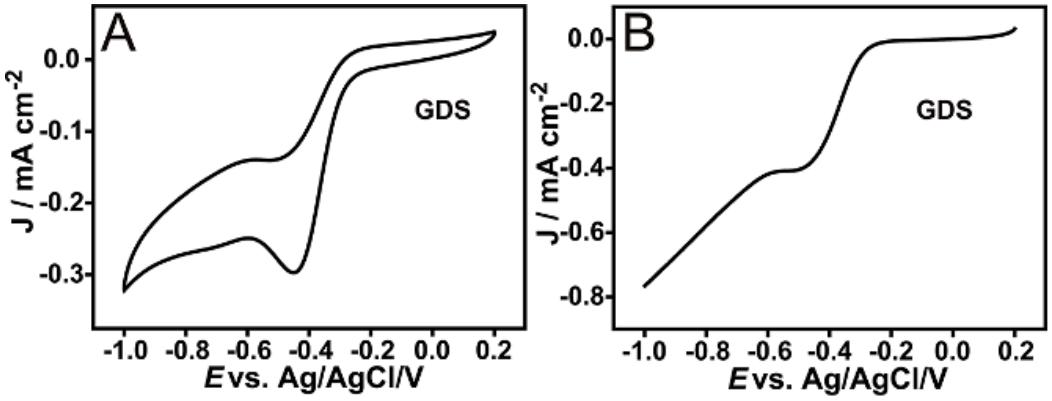

Figure S6. (A) CV curves and (B) LSV of GDS.

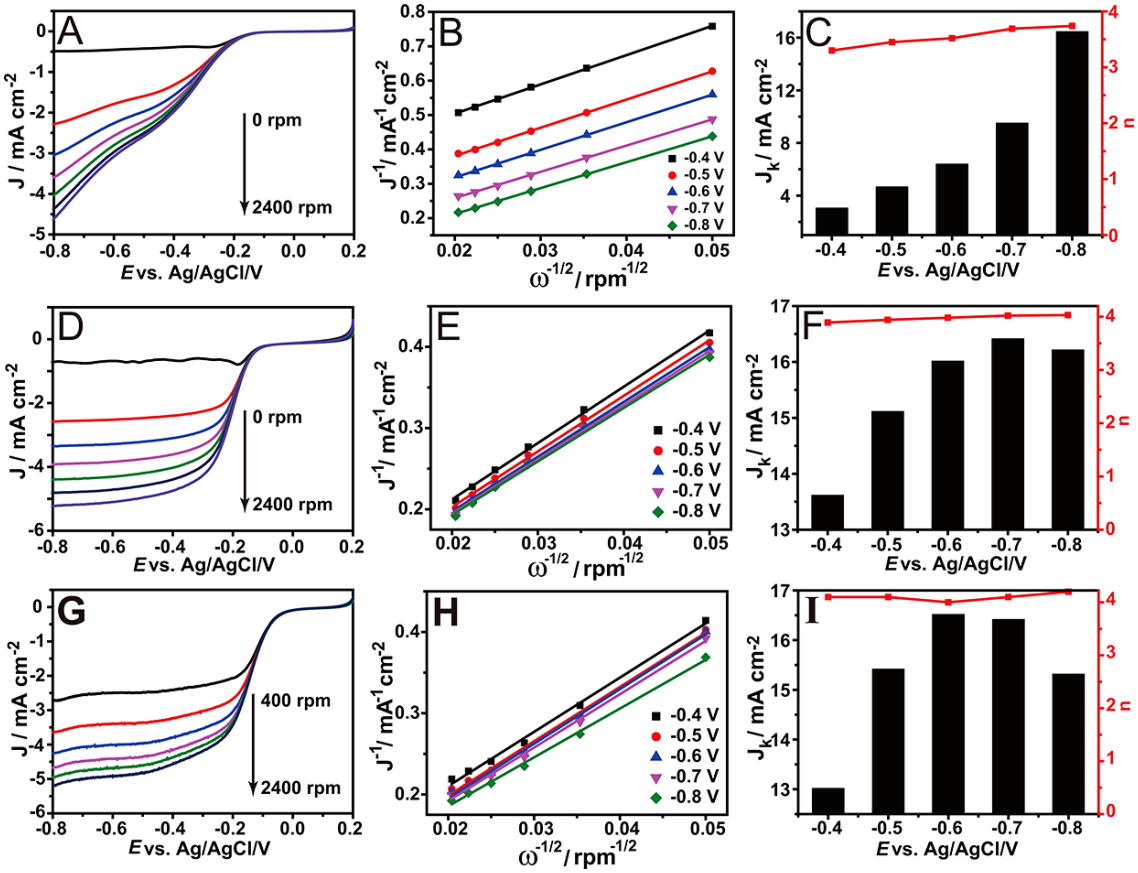

Figure S7. (A, D and G) LSVs at different rotating speeds from 0 to 2400 rpm with an increment of 400 rpm between each voltammogram, (B, E and H) K-L plots obtained at different potantials: -0.4, -0.5, -0.6, -0.7 and -0.8V and (C, F and I) kinetic limiting current density (J_k) and electron transfer number (n) calculated at different potantials. (A-C): N-CN, (D-F): N, S-CN and (G-I): Pt/C.

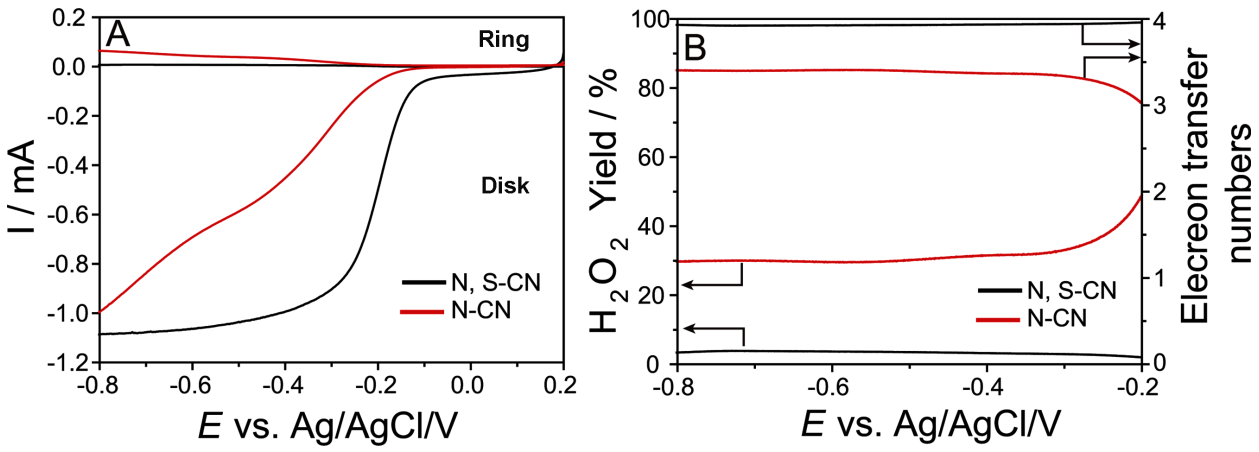

Figure S8. (A) RRDE voltammetric response in the O_2-saturated 0.1 M KOH at a scan rate of 5 mV s^{-1} and (B) H_2O_2 yields (primary Y-axis) and the corresponding electron transfer numbers (secondary Y-axis) of N, S-CN and N-CN.

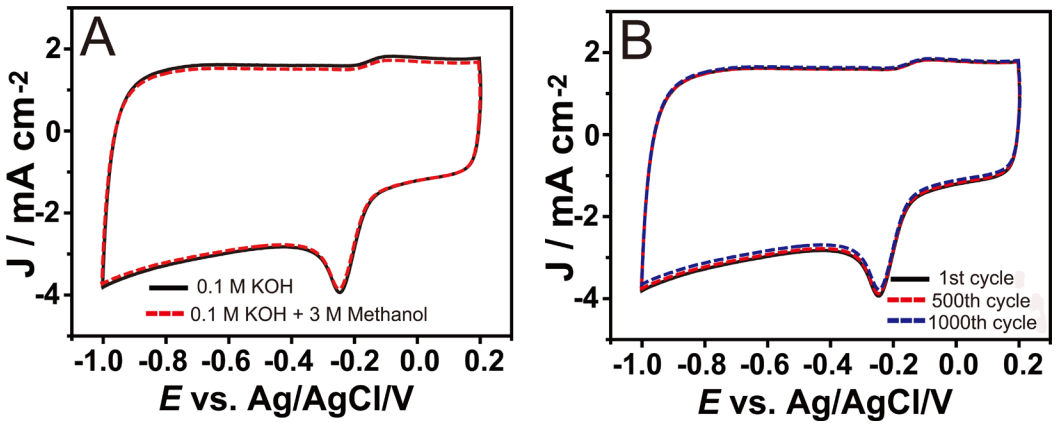

Figure S9. (A) CV curves of N, S-CN in O_2 saturated 0.1 M KOH and 0.1 M KOH + 3 M Methanol. (B) CV curves of N, S-CN in O_2 saturated 0.1 M KOH at 1st, 500th and 1000th cycle.

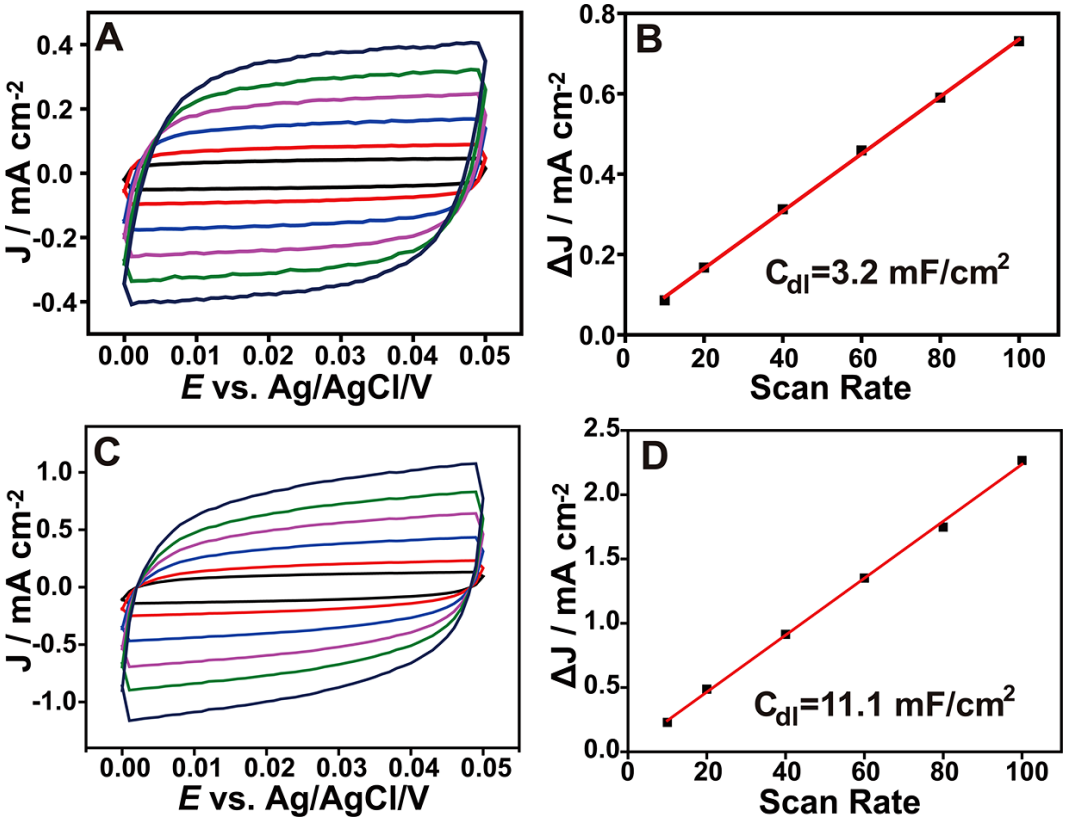

Figure S10. (A, C) CV curves at different scan rates (10, 20, 40, 60, 80 and 100 mV s^{-1}) and (B, D) the corresponding difference in the current density at 0.025 V plotted against scan rate; the calculated C_{dl} values are shown in insets. (A, B): N-CN, (C, D) N, S-CN.